Journal of Colloid and Interface Science 426 (2014) 199–205

Contents lists available at ScienceDirect

Journal of Colloid and Interface Science

www.elsevier.com/locate/jcis

Structural characterization of colloidal crystals and inverse opals using transmission X-ray microscopy

Bo-Han Huang [a], Chun-Chieh Wang [b], Chen-Hong Liao [c], Pu-Wei Wu [c,*], Yen-Fang Song [b,*]

[a] Graduate Program for Science and Technology of Accelerator Light Source, National Chiao Tung University, Hsinchu 30010, Taiwan, ROC
[b] National Synchrotron Radiation Research Center, Hsinchu 30076, Taiwan, ROC
[c] Department of Materials Science and Engineering, National Chiao Tung University, Hsinchu 30010, Taiwan, ROC

ARTICLE INFO

Article history:
Received 5 December 2013
Accepted 19 March 2014
Available online 2 April 2014

Keywords:
Transmission X-ray microscopy
Colloidal crystal
Inverse opal
Polystyrene microspheres
Electrophoresis

ABSTRACT

A nondestructive tomographic technique was used to determine the crystallographic information of colloidal crystals comprising of polystyrene (PS) microspheres, as well as their silver inverse opals. The properties of the colloidal crystals, such as defects, grain size, grain boundaries, stacking sequence, and grain orientation, were determined using the full field transmission X-ray microscopy (TXM) with a spatial resolution of 50 nm. The PS microspheres (500–750 nm) which underwent a vertical electrophoresis process to form a face-centered cubic (fcc) close-packed structure with an ABCABC packing sequence. In addition, the colloidal crystal exhibited multiple grains, and an orientation variation of 6.1° in the stacking direction between two neighboring grains.

1. Introduction

The concept of photonic crystals was first introduced by Yablonovitch [1] and John [2]. They suggested that a periodic structure with sufficient refractive index contrast can develop a photonic band gap, preventing the transmission of light of a specific wavelength. So far, numerous optical devices based on this unique characteristic have since been demonstrated. In the literatures, photonic crystals are fabricated using either top-down or bottom-up approaches [3,4]. The top-down method involves semiconductor processing, which is often expensive and time-consuming, whereas the bottom-up approach is simple and entails assembling microspheres into a close-packed array by using gravity [5,6], physical confinement [7], solvent evaporation [8,9], and electrophoresis [10]. An assembly of microspheres is known as a colloidal crystal. The filling of the interstitial voids among the microspheres followed by the selective removal of the colloidal template is defined as an inverse opal. Both colloidal crystals and their inverse opals exhibit considerable potential in applications including electrocatalysts [11], photoelectrochemical solar cells [12], electrochemical capacitors [13], and biosensors [14,15].

The crystallographic quality of colloidal crystals and their inverse opals is often diagnosed through planar and cross-sectional images from scanning electron microscopy (SEM) [16]. Due to the limited depth of penetration, SEM images are useful only for surface observations. As a result, the internal structure of the colloidal crystal (packing arrangement of the microspheres) and misorientation between neighboring grains remain unknown. Earlier, two dimensional (2D) images obtained via transmission electron microscopy (TEM) have been utilized by Cai et al. [17] to reveal multiple layers of colloidal crystals. However, a serious limitation arising from employing the TEM is the requirements of a thin sample (less than 100 nm), due to the shallow probing depth, vacuum process, and observation in a small scale. The degree of crystallization of colloidal crystals can be inferred using optical measurements [18] such as infrared (IR) reflection spectroscopy. However, the IR responses are indicative of the aggregate structural effect so localized details are still elusive.

Three-dimensional (3D) structure in a colloidal crystal has been revealed by Hilhorst et al. [19] using tomographic scanning transmission X-ray microscopy (STXM). This technique provides 30 nm spatial resolution for images with 2D absorption contrast utilizing soft X-ray with the energy of about 1.84 keV for silicon K-edge. However, the accuracy and spatial resolution of STXM tomographic reconstruction are degraded owing to the relatively low penetration power of soft X-ray, which limits the azimuthal angle range for 3D tomography data sets with only ±60° [19]. Moreover, the slow acquisition speed and large size of the data set of the STXM also compromises the resolution of tomographic reconstruction because of taking large angle steps, which is 4° in

* Corresponding authors. Fax: +886 35783813.
E-mail addresses: ppwu@mail.nctu.edu.tw (P.-W. Wu), song@nsrrc.org.tw (Y.-F. Song).

http://dx.doi.org/10.1016/j.jcis.2014.03.063
0021-9797/

their work. A full field transmission X-ray microscopy (TXM) imaging of colloidal crystals at 12 keV photon energy was demonstrated by Bosak et al. [20] with improved imaging acquisition speed and penetration depth. The TXM in Bosak's work employed the short-focus compound refractive lenses (CDL) as the objective lens. The spatial resolution is mostly determined by absorption in the lens material, hence, by choosing a more transparent material, such as Be CRL, a resolution of 100 nm is feasible. In this study, we used the full field transmission X-ray microscopy (TXM) [21,22] to investigate the 3D ultra-microstructures of colloidal crystals and their inverse opals. This TXM employs a Fresnel zone plate objective to achieve a spatial resolution of 50 nm, which is dominated by the outmost zone width and the applicable diffraction order of the zone plate, as well as a Zernike phase contrast for low atomic number samples, such as polystyrene (PS) colloidal crystals. Taking advantage of its capability for deep penetration (up to 50 μm when using an 8 keV X-ray), the TXM performs non-destructive observations of internal ultra-microstructures in an ambient environment. Here we demonstrate that the 2D TXM micrography is able to identify crystallization and defect distribution from the surface to the internal structure in colloidal crystals and their inverse opals. The 3D tomography of colloidal crystals and their inverse opals shows a layer-by-layer arrangement of the microspheres and the exact grain orientation. This novel technique allows structural relationships to be analyzed, which is impossible with other analytical instruments, and thus brings valuable insight toward the internal ultra-microstructure of colloidal crystals and inverse opals.

2. Experimental methods

A vertical electrophoresis deposition (EPD) process was adopted to direct the assembly of PS microspheres into colloidal crystals 2 cm × 2 cm × 16 μm in size. The EPD suspension was prepared by mixing 0.5 g of microspheres (500 nm or 750 nm) and 100 mL 99.5 wt% ethanol, followed by ultrasonication for 1 day. In the EPD process, an electric field of 5 V/cm to 20 V/cm was utilized to deposit microspheres onto indium tin oxide (ITO) glass substrates. Subsequently, the samples were dried at 25 °C. The resulting colloidal crystals exhibited impressive surface uniformity and a close-packed structure. A detailed process for synthesizing the PS microspheres and the electrophoretic formation of colloidal crystals were described in our previous studies [10,23]. To fabricate the inverse opals, the colloidal crystal was served as a template, allowing electroplating [24] of silver into the interstitial voids among the PS microspheres. The silver was selected because it provides a strong absorption contrast for the TXM micrograph. 0.2 M $AgNO_3$ (SHOWA) and 0.2 M citric acid (SHOWA) were used to prepare the plating electrolyte. The electroplating process was carried out in a potentiostatic mode, with the range set from 1.1 to 1.5 V. The PS microspheres were then removed using ethyl acetate, producing a silver skeleton with interconnected channels.

The TXM facility [21] of beamline BL01B [22] at the National Synchrotron Radiation Research Center (NSRRC) in Hsinchu, Taiwan provides 2D micrograph and 3D tomography at spatial resolutions of 50 nm, with first-order diffraction of a Fresnel zone plate at an X-ray energy of 8 keV. The field of view of the image is 15 × 15 μm^2 for the first-order diffraction of the zone plate. A millimeter-scale field of view of the sample can be generated by stitching images from a series of observation positions. After acquiring a series of 2D micrographs with the sample rotated stepwise azimuthally, the 3D tomography data sets were reconstructed by applying a filtered back-projection algorithm based on 181 sequential image frames taken with the azimuth angle rotating from −90° to +90°. The final 3D tomography structures were generated using Amira 3D software to enhance the visualization.

3. Results and discussion

3.1. SEM imaging analysis of PS colloidal crystals and silver inverse opals

Fig. 1 exhibits the SEM images of the colloidal crystal. Fig. 1a is a top view, showing the assembly of PS microspheres (500 nm in diameter) in grains of 80 μm × 105 μm, along with the presence of grain boundaries and vacancies. Fig. 1b is a cross-sectional view, showing a layer-by-layer structure revealing a close-packed arrangement. Defects such as vacancies and voids were clearly observed, but these might have been produced during the electrophoresis process or were caused simply when breaking the sample for SEM cross-sectional observation. Moreover, the grain orientation and packing sequence were not discernible, which is a persistent problem in the field.

Fig. 2a and b display the top and cross-sectional views of the silver inverse opal fabricated using the colloidal crystal template in Fig. 1. The inverse opal structure consisted of interconnected voids in a hexagonal pattern, and its morphology was similar to that of the colloidal crystal. Both colloidal crystals and inverse opals exhibited excellent crystallinity, and they provided perfect models for structural characterization by TXM.

3.2. Crystallinity and defects characterization by 2D TXM micrograph

Fig. 3a demonstrates the 2D TXM micrograph of a colloidal crystal comprised of PS microspheres with a diameter of 750 nm. The PS microspheres are the areas in dark contrast, owing to their stronger X-ray absorption compared with that of air. Fig. 3b displays the 2D TXM micrograph of an inverse opal generated from

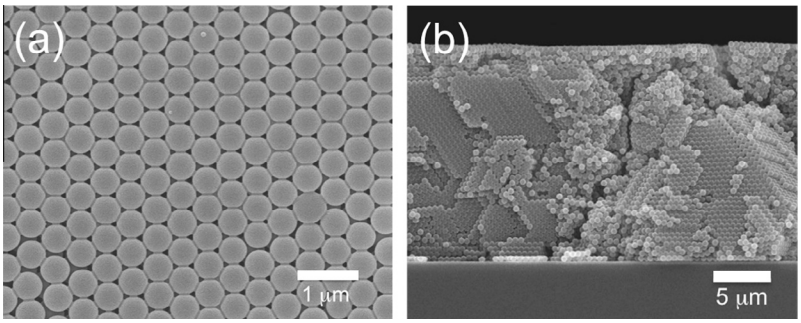

Fig. 1. SEM images of a polystyrene-based (PS) colloidal crystal which underwent a vertical electrophoresis process. (a) Top view, showing the assembly of PS microspheres (500 nm in diameter). (b) Cross-sectional view, showing a layer-by-layer structure in a close-packed arrangement, as well as grain boundaries. These colloidal crystals exhibit excellent crystallinity.

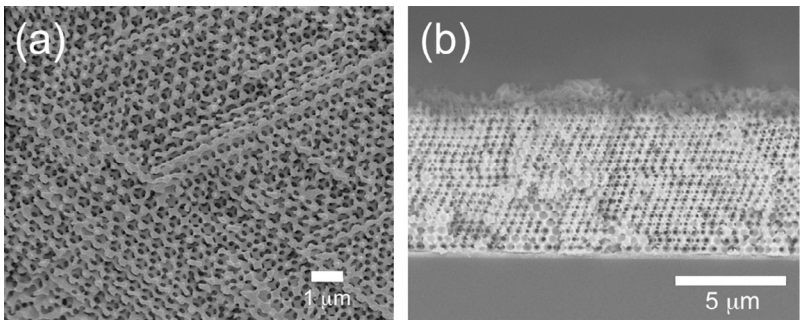

Fig. 2. SEM images of silver inverse opals fabricated using the colloidal crystal template in Fig. 1. (a) Top view, (b) Cross-sectional view. The inverse opal structure consists of interconnected voids in a hexagonal pattern, showing the excellent crystallinity of the PS colloidal crystal.

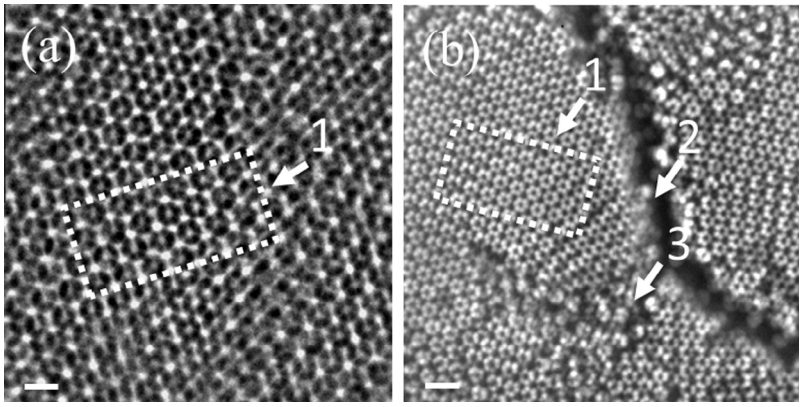

Fig. 3. Internal structures of the PS colloidal crystal and silver inverse opal from 2D TXM micrographs. The scale bar represents 1 μm. (a) PS colloidal crystal with a microsphere diameter of 750 nm. The PS microspheres are the areas in dark contrast. (b) Silver inverse opal fabricated using the colloidal crystal template with a microsphere diameter of 500 nm. The areas in light contrast represent the voids left by the PS microspheres. Arrow #1 shows the close-packed region. Arrow #2 shows the grain boundary. Arrow #3 indicates the defects.

the PS microspheres with a diameter of 500 nm. The areas in light contrast represent the voids left by the PS microspheres.

Arrow #1 in Fig. 3a and b indicates the close-packed structure in the colloidal crystal and inverse opal. These particular patterns will be discussed in later figures. In addition, the grain boundary is clearly defined, as shown in the area marked by Arrow #2 in Fig. 3b. Furthermore, owing to the non-destructive nature of TXM, the defect area (Arrow #3, Fig. 3b) produced during the crystal formation process was successfully identified via a 2D TXM micrograph.

The areas indicated by the Arrow #1 in Fig. 3a and b are shown in Fig. 4a and b, respectively. Fig. 4c and d display the corresponding simulations of the close-packed structure in the colloidal crystal and inverse opal. Both sets of figures are labeled with a numerical analysis. The distances a, b, c, and d shown in Fig. 4a, as well as a′, b′, c′, and d′ shown in Fig. 4b were obtained using direct measurements, whereas the corresponding distances in Fig. 4c and d were estimated from an ideal close-packing structure. The variations between the simulated theoretical values and the TXM-determined results are less than 7%. This deviation is attributed to the size variation of the PS microspheres, as well as the stacking stability. The small deviation proves that the ordered patterns in Fig. 4a and b represent colloidal crystals and inverse opals with excellent crystallinity. In addition, a 2D TXM micrograph is a transmission X-ray microscopic image that elucidates the multilayer structure of a sample. Hence, the close-packed structure (the areas marked by the Arrow #1 in Fig. 3a and b) can be characterized precisely and quickly by comparing the observed images and simulation results. In short, the non-destructive nature of 2D TXM micrograph enables the accurate determination of crystallographic information such as defects, grain sizes, and grain boundaries.

3.3. Stacking sequence identification of colloidal crystals by 3D TXM tomography

In general, microspheres in a close-packed colloidal crystal might adopt two distinct packing orders; face-centered-cubic (fcc) with an ABCABC stacking sequence, or hexagonal-close-packed (hcp) with an ABABAB stacking sequence. The determination of the stacking sequence within a colloidal crystal by using cross-sectional SEM images is unlikely because breaking the sample might disrupt the packing sequence. In this study, 3D TXM tomography of a colloidal crystal was used to elucidate the exact stacking sequence of four layers of PS microspheres. Fig. 5a–d exhibits the first to the fourth layer of the assembled PS microspheres. We utilized the ‘‘Amira’’ software to observe the stacking sequence of the reconstructed 3D tomography of a PS colloidal crystal. In order to identify individual stacking layer, we used a slicing plane which was parallel to the stacking layers to observe the 2D sectioned image inside the PS colloidal crystal. By moving this slicing plane along the stacking direction, we could observe the stacking sequence layer by layer. The diameter of the sectioned PS microspheres reached the maximum value as the slicing plane was located at the center of the microspheres. At this stage, the individual layer was recognized. To identify the selected PS microsphere, we recorded the scanning layers process of the slicing plane in a movie. Then, the film-editing software was used

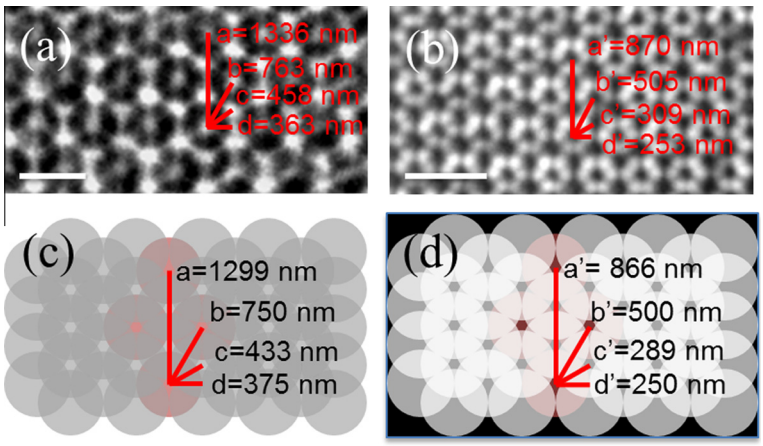

Fig. 4. Comparison of the internal structures of the PS colloidal crystal and the silver inverse opal using 2D TXM micrographs, with corresponding simulations of the closed-packed structure. The scale bar represents 1 μm. (a) 2D TXM micrograph of the PS colloidal crystal. (b) 2D TXM micrograph of the silver inverse opal. (c) Simulated closed-packed structure projection pattern of the colloidal crystal. (d) Simulated closed-packed structure projection pattern of the inverse opal. Variations in distance (a, b, c, d shown in Figs. 4a, c, and a′, b′, c′, d′ shown in Fig. 4b and d) between the TXM-determined results and the corresponding simulated theoretical values are less than 7%.

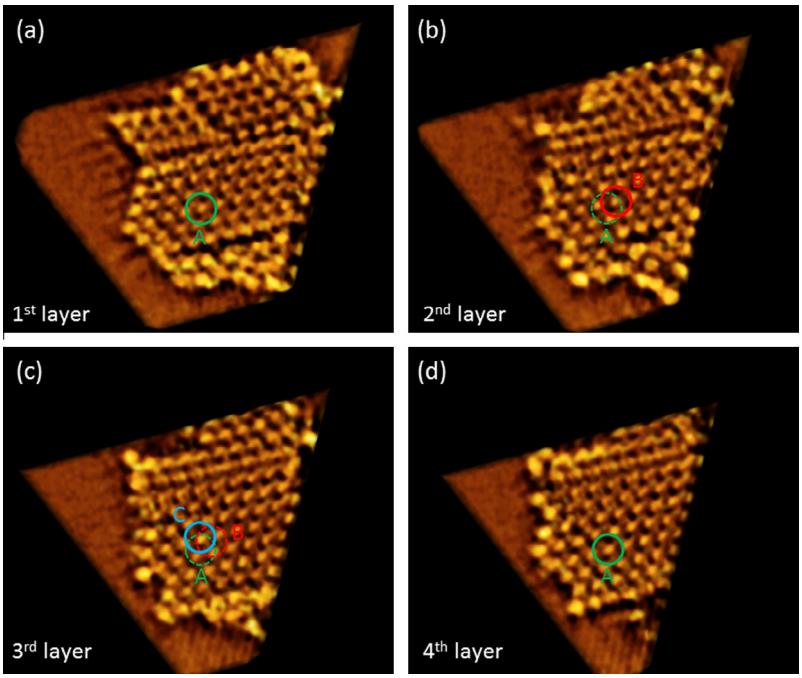

Fig. 5. 3D TXM tomography of the PS colloidal crystal. (a) The first layer of PS microspheres. The position of the selected PS microsphere for observation was located at the center of the green circle A. (b) The second layer of PS microspheres. No PS microsphere fitted to the center of the green circle A. We marked the PS microsphere, which was the closest one to the center of green circle A, located at the center of the red circle B. (c) The third layer of PS microspheres. Similarly, no PS microsphere fitted to the centers of green circle A and red circle B. We marked the PS microsphere, which was the closest one to the centers of green circle A and red circle B, located at the center of the blue circle C (d) The fourth layer of PS microspheres. There appeared one PS microsphere which fitted to the center of green circle A as in (a). This pattern conforms to an ABCA sequence, indicating an fcc structure. (For interpretation of the references to color in this figure legend, the reader is referred to the web version of this article.)

to mark one of the PS microspheres. The marked microsphere was located in the center of the green circle A in the first layer as shown in Fig. 5a. As the slicing plane was moved continuously and gradually to the second layer, we discovered that none of the PS microspheres in this layer could fit to the center of the green circle A. This means that the stacking location of the second layer is different from the first layer. We then marked the PS microsphere, which was the closest one to the center of green circle A, located at the center of the red circle B in the second layer (as shown in Fig. 5b). Similarly, we observed that the stacking location in the third layer was different from the first and second layer. Again we marked the PS microsphere, which was the closest one to the centers of circles green A and red B, located at the center of the blue circle C in the third layer (as shown in Fig. 5c). Finally, when the slicing plane was moved to the fourth layer, there appeared one PS microsphere which fitted to the center of green circle A (as shown in Fig. 5d). This means that the stacking location of the forth layer was identical to the first layer. The tomographic movie of Fig. 5a–d is shown in Supplemental figure Fig. S1. This pattern conforms to an ABCA sequence, indicating an fcc structure. Therefore, in our case, the electrophoresis of PS microspheres produced a colloidal crystal with an fcc close-packed arrangement in an ABCABC

stacking sequence, instead of an ABABAB hexagonal array. This technique enables the exact determination of the stacking sequence of a colloidal crystal.

3.4. Determination of grain orientation of the colloidal crystals

To precisely determine the grain orientation of the colloidal crystals, a 3D TXM tomography was employed on the silver inverse opals. This approach provides a superior contrast as compared to 3D tomography on the PS colloidal crystals. In this case, the X-ray was transmitted through the thinnest part of the silver skeleton (less than 50 nm thick). Using an 8 keV X-ray, the transmittance of the 50 nm thick silver reached 0.989, yielding almost complete transparency. Consequently, the 3D tomography of four layers of the inverse opal revealed a honeycomb-like structure, as shown in Fig. 6a and b. Two distinct grains on the top view (rotating azimuth angle of 0°) tomography image are indicated by dashed-line and solid-line circles in Fig. 6a. The dashed-line circle (Grain #1) exhibits a standard inverse opal pattern in the (1 1 1) plane (black holes with light spots in the middle, as shown in Fig. 6c), indicating that the growth direction of Grain #1 is parallel to the normal of the substrate, which is often expected in the self-assembly of colloidal microspheres. However, the solid-line circle (Grain #2) shows a pattern of black holes with light rods in the middle with an unknown direction of growth, indicating an alternate growth direction in this structure. To analyze the grain orientation of Grain #2, a bi-axial rotation was employed (inset of Fig. 6b) to allow this grain to align with the pattern of the (1 1 1) plane. After using the bi-axial rotation (X axis = 5.5°, Y axis = 2.7°, Z axis, which is parallel to our observation of the screen, is fixed), it was not only possible to determine the pattern of Grain #2 in the (1 1 1) plane in Fig. 6b (where the pattern of Grain #1 had disappeared), but the tilting angle (δ) between the normal direction of the substrate and the orientation of Grain #2 could also be calculated using Eq. (1):

$$\cos\delta = \cos\theta \cdot \cos\sigma \tag{1}$$

Substituting with the rotation angles, the θ of the X axis and the σ of the Y axis, the δ of Grain #2, became 6.1°. To confirm this analysis, a 3D simulation of the inverse opal was performed using MATLAB (Fig. 6c and d). Fig. 6c displays the 3D simulation of the inverse opal with the (1 1 1) surface normal to the incident X-ray direction. This pattern was consistent with both the simulation in Fig. 4d and the 2D TXM micrograph of the silver inverse opal in Fig. 4b. The inverse opal surface in Fig. 6d was rotated from the (1 1 1) plane to the plane with the corresponding azimuth angle via rotation of −5.5° about the X axis and −2.7° about the Y axis, yielding a tilting angle of 6.1°, after application of Eq. (1). The pattern in Fig. 6d was obtained, which is the same as the pattern in the solid-line circle in Fig. 6a. This proves that grain orientation can be clearly analyzed using 3D TXM tomography.

This observation also confirmed that in a colloidal crystal, even close-packed grains might adopt slightly different packing orientations. Orientation variation in a close-packed region cannot be distinguished using a top view SEM image, as it does not reveal noticeable orientation differences. Orientation variance may not be readily apparent even when cross-sectional SEM images are adopted. Fig. 7 illustrated a SEM image with three grains in slightly different orientations. Assuming the ITO substrate is located in the X–Y plane (see the coordinates in the insets of Fig. 7a and b), the

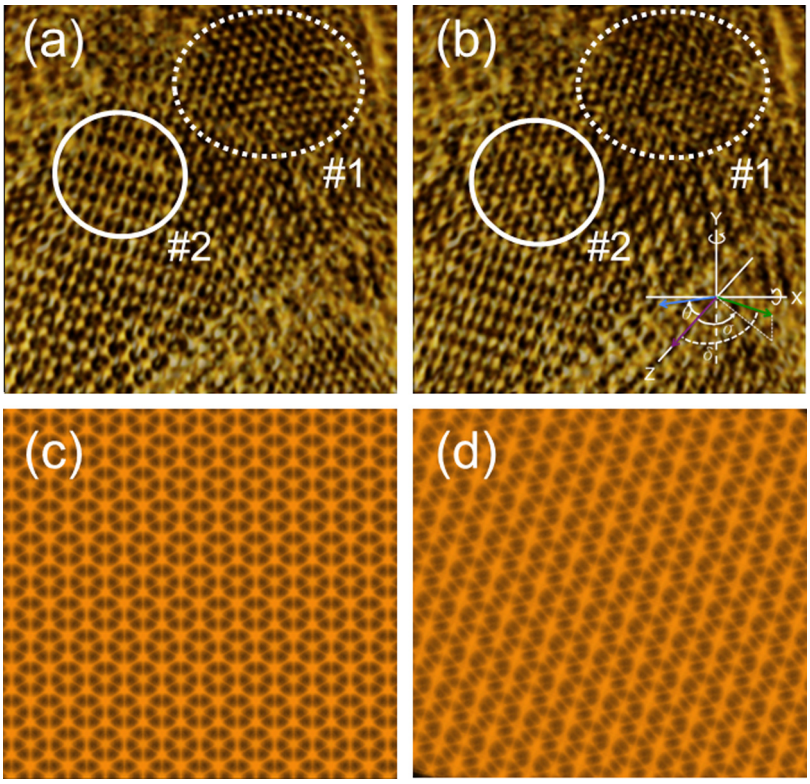

Fig. 6. 3D TXM tomography and simulation of the silver inverse opal. (a) Top view of the 3D TXM tomography of the silver inverse opal. Two areas with distinctly different structures were observed, and marked by the dashed-line circle (grain #1) and the solid-line circle (grain #2). Grain # 1 exhibits the standard inverse opal pattern in the (1 1 1) plane (black holes with light spots in the middle), which is shown in (c). Grain #2 shows a pattern of black holes with light rods in the middle with an unknown direction of growth (b) The structure in (a) after bi-axial rotation (of X axis = 5.5°, Y axis = 2.7°). Grain #2 exhibits the pattern of (1 1 1) plane as the pattern in (c). (c) 3D simulation of the top view of the inverse opal with an fcc close-packed structure in (1 1 1) plane. (d) 3D simulation of the structure in (c) after bi-axial rotation (of X axis = -5.5°, Y axis = -2.7°) exhibits the pattern of grain #2 in (a).

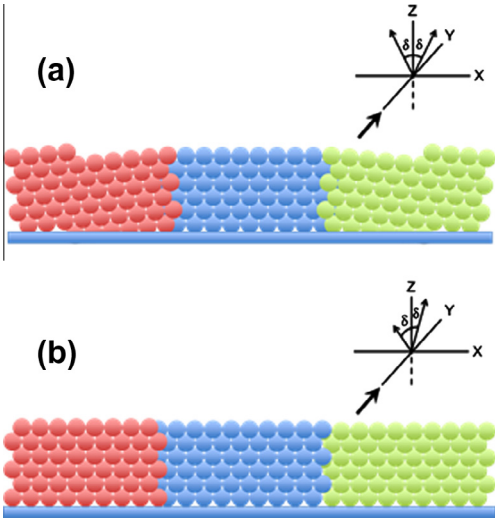

Fig. 7. Simulation of three grains with different orientations, mimicking cross-sectional SEM images. Assuming the ITO substrate is located in the *X*–*Y* plane (see the coordinates in insets (a) and (b)), the orientation of the blue grain is in the direction of the *Z*-axis, while the other two grains (red and green grains) have orientation variances of $\delta = 6.1^\circ$ with respect to the *Z*-axis direction. (a) The tilting orientations of the red grain and green grain are in the *X*–*Z* plane and at symmetric sites (thin arrows in the inset). If these grains are observed from the *Y*-axis (thick arrow in the inset), the orientation variance can be distinguished. (b) The tilting orientations of the red grain and green grain are in the *Y*–*Z* plane, and at symmetrical sites (thin arrows in the inset). If these grains are observed from the *Y*-axis (thick arrow in the inset), as in (a), it is nearly impossible to distinguish the orientation variance. (For interpretation of the references to color in this figure legend, the reader is referred to the web version of this article.)

orientation of the blue grain is in the *Z*-axis direction, whereas the other two grains (red grain and green grain) have an orientation variance of $\delta = 6.1^\circ$ with respect to the *Z*-axis direction. Fig. 7a shows that the tilting orientations of the red and green grains are in the *X*–*Z* plane, and at symmetric sites (thin arrows in the inset). If these grains are observed from the *Y*-axis (thick arrow in the inset), the orientation variance can be distinguished. Fig. 7b shows that the tilting orientations of the red and green grains are in the *Y*–*Z* plane, and at symmetric sites (thin arrows in the inset). If these grains are observed from the *Y*-axis (thick arrow in the inset), as in Fig. 7a, it is nearly impossible to distinguish the orientation variance. Fig. 7a shows the most obvious tilting direction of the grain. However, the exact grain orientation cannot be determined because it is a 2D image, and cannot be used to accurately define the 3D orientation. Moreover, the structure is disrupted by breaking the sample for cross-sectional SEM observation. Fig. 7b shows the most obscure tilting direction of the grain. In this scenario, it is evident that very few differences can be observed between the three hypothetical grains.

The cross-sectional SEM image shown in Fig. 8 displays the close-packed structures fabricated by the electrophoresis process from our laboratory, and reveals a minute difference in grain orientation. The arrow bars indicate two grains with different orientations, and the tilting angle can be obtained after careful observation. However, the cross-sectional SEM image provides only limited information, and cannot be used to accurately identify variances in 3D orientation. For example, in Fig. 8, the left grain exhibits some degree of tilting, but it cannot be ascertained whether the grain tilted toward or away from the image plane. Moreover, it is rather difficult to identify a grain normal to the substrate, i.e. one without tilting in any orientation, because it is impossible to observe the tilting angle of a grain in every direction using the 2D SEM images.

Therefore, 3D TXM tomography is a powerful new tool to distinguish distinct stacking orientations among the grains in a colloidal crystal and inverse opal. This helps to shatter the conventional assumption that the only stacking orientation in a close-packed colloidal crystal is normal to the substrate.

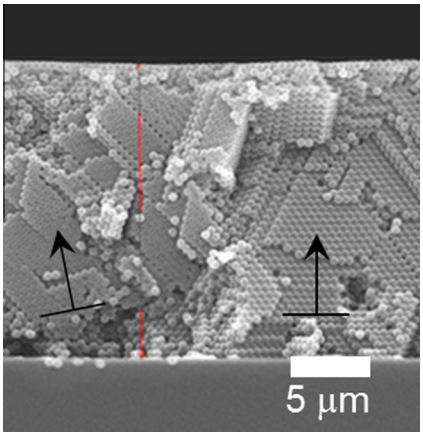

Fig. 8. A cross-sectional SEM image of a close-packed PS colloidal crystal fabricated by our laboratory reveals few noticeable differences in grain orientation. The arrow bars indicate two grains with different orientations, and the tilting angle can be obtained after careful observation. However, the cross-sectional SEM image provides only limited information, and cannot be used to accurately identify variances in the 3D orientation.

4. Conclusion

In summary, colloidal crystals consisting of PS microspheres were prepared using a vertical electrophoresis process, and silver inverse opals were fabricated using the PS colloidal crystals as a template. TXM provides an unprecedented analytical method for non-destructively determining the internal structure of colloidal crystals and inverse opals. Crystallographic ordering, defects, and crystal quality were observed using 2D TXM micrograph. Furthermore, 3D TXM tomography precisely revealed the stacking sequence and grain orientation. The experimental data confirmed that the colloidal crystal adopted an fcc close-packed arrangement in an ABCABC sequence, and contained multiple grains with an orientation variance of 6.1° in the stacking direction between two neighboring grains. These results provide new insight into the relationship between optical properties and crystallographic structures, and are valuable in guiding the crystal formation process.

Acknowledgments

We thank the staff of the NSRRC for their assistance and Professor Yeu-Kuang Hwu at Institute of Physics, Academia Sinica for his help. This work was partially supported by the Graduate Program for Science and Technology of Accelerator Light Source of NSRRC and National Chiao Tung University and the National Science Council of Taiwan (Contract No. NSC 102-2112-M-213-001-MY3).

Appendix A. Supplementary material

Supplementary data associated with this article can be found, in the online version, at http://dx.doi.org/10.1016/j.jcis.2014.03.063.

References

[1] E. Yablonovitch, Phys. Rev. Lett. 58 (1987) 2059.
[2] S. John, Phys. Rev. Lett. 58 (1987) 2486.
[3] M. Campbell, D.N. Sharp, M.T. Harrison, R.G. Denning, A.J. Turberfield, Nature 404 (2000) 53.
[4] Hailin Cong, Bing Yu, Jianguo Tang, Zejing Li, Xuesong Liu, Chem. Soc. Rev. 42 (2013) 7774.

[5] P.G. Ni, P. Dong, B.Y. Cheng, X.Y. Li, D.Z. Zhang, Adv. Mater. 13 (2001) 437.
[6] M. Murai, T. Okuzono, M. Yamamoto, A. Toyotama, J. Yamanaka, J. Colloid Interface Sci. 370 (2012) 39.
[7] B. Gates, D. Qin, Y.N. Xia, Adv. Mater. 11 (1999) 466.
[8] Z.Y. Zheng, X.Z. Liu, Y.H. Luo, B.Y. Cheng, D.Z. Zhang, Q.B. Meng, Y.R. Wang, Appl. Phys. Lett. 90 (2007) 051910.
[9] M.H. Kim, H.K. Choi, O.O. Park, S.H. Im, Appl. Phys. Lett. 88 (2006) 721.
[10] Y.J. Huang, C.H. Lai, P.W. Wu, Electrochem. Solid-State Lett. 11 (2008) 20.
[11] G.Q. Guan, R. Zapf, G. Kolb, Y. Men, V. Hessel, H. Loewe, J.H. Ye, Chem. Commun. (2007) 260.
[12] I. Rodriguez, P. Atienzar, F. Ramiro-Manzano, F. Meseguer, A. Corma, H. Garcia, Phot. Nano. Fund. and Appl. 3 (2005) 148.
[13] K.C. Liu, M.A. Anderson, J. of Electrochem. Soc. 143 (1996) 124.
[14] Y. Bai, W.W. Yang, Y. Sun, C.Q. Sun, Sens. Actuators B-Chem. 134 (2008) 471.
[15] You Xueqiu, J.H. Pikul, W.P. King, J.J. Pak, Appl. Phys. Lett. 102 (2013) 253103.
[16] N. Pérez, A. Hüls, D. Puente, W. González-Viñas, E. Castaño, S.M. Olaizola, Sens. Actuators B: Chemical 126 (2007) 86.
[17] Z. Cai, J. Teng, Y. Wan, X.S. Zhao, J. Colloid Interface Sci. 380 (2012) 42.
[18] N.P. Johnson, D.W. McComb, A. Richel, B.M. Treble, R.M. De la Rue, Synth. Met. 116 (2001) 469.
[19] J. Hilhorst, M.M. van Schooneveld, J. Wang, E. de Smit, T. Tyliszczak, J. Raabe, A.P. Hitchcock, m. Obst, F.M.F. de Goot, A.V. Petukhov, Langmuir 28 (2012) 3614.
[20] A. Bosak, I. snigireva, K.S. Napolskii, A. Snigirev, Adv. Mater. 22 (2010) 3256.
[21] G.C. Yin, M.T. Tang, Y.F. Song, F.R. Chen, K.S. Liang, F.W. Duewer, W.B. Yun, C.H. Ko, H.P.D. Shieh, Appl. Phys. Lett. 88 (2006) 241115.
[22] Y.F. Song, C.H. Chang, C.Y. Liu, S.H. Chang, U.S. Jeng, Y.H. Lai, D.G. Liu, S.C. Chung, K.L. Tsang, G.C. Yin, J.F. Lee, H.S. Sheu, M.T. Tang, C.S. Hwang, Y.K. Hwu, K.S. Liang, J. Synchrotron Rad. 14 (2007) 320.
[23] Yi-Jui Huang, Chun-Han Lai, Wu Pu-Wei, Li-Yin Chen, Mater. Lett. 63 (2009) 2393.
[24] G.M. Zarkadas, A. Stergiou, G. Papanastasiou, Electrochim. Acta 50 (2005) 5022.